FRONT MATTER

23 Title

1

4 Charge-Clustering Induced Fast Ion Conduction in 2LiX-GaF₃: A Novel Strategy for Electrolyte

5 Design

67 Authors

- 8 Sawankumar V. Patel^{1,2,†}, Valentina Lacivita^{3,*,†}, Haoyu Liu^{1,†}, Erica Truong¹, Yongkang Jin¹,
- 9 Eric Wang³, Lincoln Miara^{3,#}, Ryounghee Kim⁴, Hyeokjo Gwon⁴, Rongfu Zhang^{1,2}, Ivan Hung²,
- Zhehong Gan², Sung-Kyun Jung^{4,5,*}, Yan-Yan Hu^{1,2,*}

12 **Affiliations**

- ¹Department of Chemistry and Biochemistry, Florida State University, Tallahassee, FL 32306,
- 14 USA.

11

13

15

21

25

26

272829

30

31 32

33

34

35

36

37

38

39

40

41

42

43

44 45

46

47 48

- ²Center of Interdisciplinary Magnetic Resonance, National High Magnetic Field Laboratory, 1800
 East Paul Dirac Drive, Tallahassee, FL 32310, USA.
- ³Advanced Materials Lab, Samsung Advanced Institute of Technology-America, Samsung
 Semiconductor, Inc., Cambridge, Massachusetts 02138, USA.
- ⁴ Battery Material Lab, Material Research Center, Samsung Advanced Institute of Technology
 (SAIT), Samsung Electronics Co., Ltd., 130 Samsung-ro, Yeongtong-gu, Suwon-si, Gyeonggi-do,
 16678 Republic of Korea
 - ⁵ School of Energy and Chemical Engineering, Ulsan National Institute of Science and Technology (UNIST), 50 UNIST-gil, Ulsan, 44919 Republic of Korea
 - *Currently at Pure Lithium Corporation
 - *Corresponding Authors. Dr. Sung-Kyun Jung, Email: skjung@unist.ac.kr; Dr. Yan-Yan Hu, Email: yhu@fsu.edu

Abstract

2LiX-GaF₃ (X = Cl, Br, I) electrolytes offer unique features for solid-state batteries: mechanical pliability and high conductivities. However, understanding the origin of fast ion transport in 2LiX-GaF₃ has been challenging. Surprisingly, the ionic conductivity order of 2LiCl-GaF₃ (3.2 mS/cm) > 2LiBr-GaF₃ (0.84 mS/cm) > 2LiI-GaF₃ (0.032 mS/cm) contradicts binary LiCl (10⁻¹² S/cm) < LiBr (10⁻¹⁰ S/cm) < LiI (10⁻⁷ S/cm). Using multinuclear ⁷Li, ⁷¹Ga, ¹⁹F solid-state NMR and DFT simulations, we found that Ga(F,X)n polyanions boost Li⁺-ion transport by weakening Li⁺-X⁻ ionic interactions via charge clustering. In 2LiBr-GaF₃ and 2LiI-GaF₃, Ga-X coordination is reduced with deceased F participation in polyanion formation, compared to 2LiCl-GaF₃. These insights guide high-performance electrolyte design based on charge clustering, applicable to various ion conductors: liquid, polymer, and glass-ceramics. This new strategy could prove effective for producing highly conductive multivalent cation conductors such as Ca²⁺ and Mg²⁺, as charge clustering of carboxylates in proteins has been found to decrease their binding to Ca²⁺ and Mg²⁺.

49 **Teaser**

MAIN TEXT

Introduction

High-performance inorganic solid electrolytes are indisputably crucial to the transition of current rechargeable Li⁺-ion batteries that use liquid electrolytes to all-solid-state batteries (ASSBs) for both enhanced safety and high energy density. A repertoire of properties has been considered to design solid electrolyte for successful integration in ASSBs, namely ionic conductivity, air/water stability, electrode compatibility over extended temperature and voltage range, and mechanical pliability. Various solid electrolytes have been developed in attempts to satisfy those criteria. Superionic conductors with conductivities on the order of ~10 mS/cm, even surpassing the ionic conductivity of state-of-the-art liquid electrolytes, have been developed in sulfide-based chemical spaces. Prominent examples of these materials are argyrodite and thio-LISICON electrolytes. Chemical stability against both Li metal and air exposure has also been achieved in oxide-based solid electrolytes, such as garnets. Other solid electrolytes such as hydrides or halides present excellent reduction and oxidation stability, respectively. Other solid electrolytes such as hydrides or halides present excellent reduction and oxidation stability, respectively.

Currently, a core issue of ASSBs is the mechanical, chemical, and electrochemical compatibility of solid electrolytes with electrodes. Non-conformal contact at the electrode-electrolyte interface has shown to limit the power density and induces dendrite formation in ASSBs. Most sulfide, oxide, halide solid electrolytes often need a high stack pressure (a few MPa) or a co-sintering process for ASSB fabrication and operation. However, these strategies seem inadequate to maintain physical integrity given the reversible volume change of electrodes upon electrochemical cycling. Therefore, to avoid dynamic mechanical degradation, the design of high-performance solid electrolytes should also take into account of physical deformability, which is required to accommodate stress and strain evolution at the interface. 16, 21, 22

Recently developed Ga-based mixed-halide solid electrolytes could be a valuable venue to address the interface issues due to promising characteristics including high ionic conductivity and physical pliability. Indeed, these materials exhibit high ionic conductivity over 3 mS/cm and clay-like mechanical properties, corresponding to complex shear moduli of $10^5 \sim 10^6$ Pa, which enable the ASSBs to operate without stack pressure to maintain conformal cathode-electrolyte interface contact over extended stable electrochemical cycling. Although it is vaguely understood from the synthesis perspective that the unique features of these new solid electrolytes can be observed only when mixed halide anions are incorporated, their amorphous structure with the absence of long-range ordering makes it challenging to trace the structural origin of fast ion transport.

Here, in order to elucidate the short-range structures in clay-like solid electrolytes and their correlation with the ion transport, we have performed combined analyses using X-ray diffraction (XRD), solid-state nuclear magnetic resonance (NMR), and density functional theory (DFT) calculations on systems with reference stoichiometry 2LiX-GaF_3 (X=Cl, Br, I). We reveal that the identity of X anions has a significant effect on the observed Li⁺-ion conductivity. Indeed, the conductivity is 3.2 mS/cm when X = Cl and is reduced by a factor \sim 4 for X = Br ($8.39 \times 10^{-1} \text{ mS/cm}$) and by about 100 times for X = I ($3.04 \times 10^{-2} \text{ mS/cm}$). We have identified the formation of complex $\text{GaCl}_m F_{n-m}$ polyanions in 2LiCl-GaF_3 , and consequent diversification of the Li⁺ local environments, as a major factor in promoting fast ion transport by limiting strong Li-F ionic interactions that can slow down Li⁺ transport. More generally, in drawing a parallel with the concept of "charge clustering", well-known in biochemistry, ²⁴ the Ga(X,F)n polyanions forming the 2LiX-GaF_3 amorphous framework may be conceived as gallium-centered clusters where multiple

negatively charged anions (F and X halides) are attracted to a central gallium cation. Such negative charge clustering in gallium-based polyanions screens interactions between positive charge carriers and negative hosts, therefore weakening Li⁺ binding affinity for fast ion transport. In contrast, Br and I tend to displace F from its interactions with Ga, thus limiting the charge clustering screening effect on the Li⁺-ion conduction. This study enriches our understanding of amorphous solid electrolytes and provides further insight for designing highly conductive clay-like ion conductors.

Results

The amorphous character of 2LiX-GaF₃

X-ray powder diffraction was used to identify crystalline phases present in the 2LiX-GaF₃ (X = Cl, Br, I) samples. **Error! Reference source not found.**a compares powder X-ray patterns of the 2LiX-GaF₃ compounds and the precursor GaF₃. All three mixed halide compositions display only weak crystalline peaks that are largely overridden by a broad, dominant background, revealing that the major phases are highly disordered. The absence of Bragg peaks from precursors GaF₃ and LiX also indicates that chemical reactions have taken place to transform them into new phases. An attempt to match the weak Bragg peaks in 2LiX-GaF₃ was conducted by performing a search match with the available phases in the Inorganic Crystal Structure Database (ICSD) as shown in **Error! Reference source not found.**b-d. The phases that matched with the weak crystalline peaks in 2LiCl-GaF₃ are Li₃GaF₆ (ICSD ID: 409384) and LiGaCl₄ (ICSD ID: 60849). In 2LiBr-GaF₃ and 2LiI-GaF₃, the diffraction peaks matched LiGaBr₄ (ICSD ID: 61337) and LiGaI₄ (ICSD ID: 60850), respectively. The above-mentioned crystalline peaks may hint at the presence of local structures having characteristics similar to the Li₃GaF₆ and LiGaX₄ (X = Cl, Br, I) structures. However, due to the poor crystallinity of the 2LiX-GaF₃ samples, powder XRD was insufficient to provide more detailed phase or structure information.

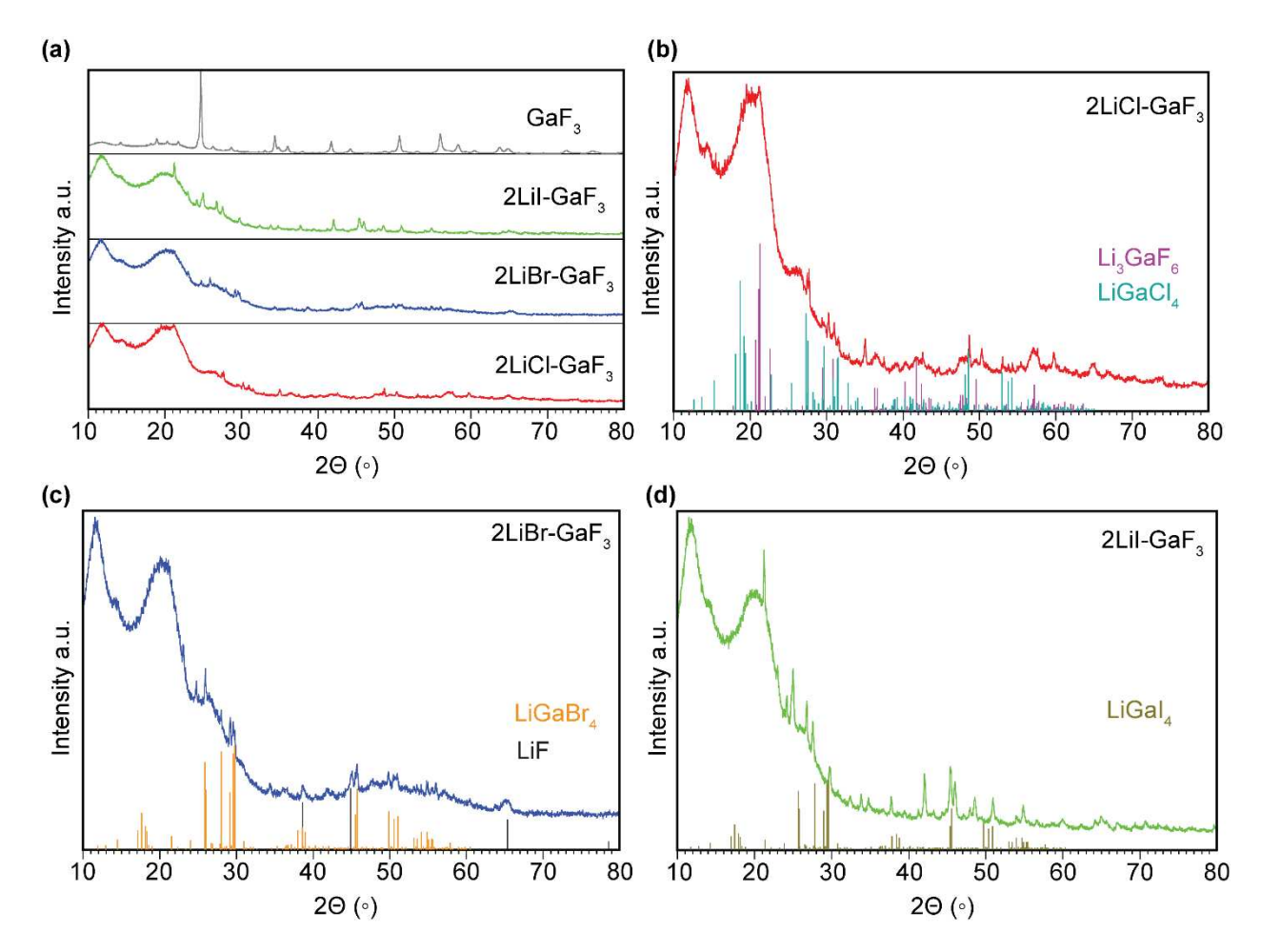


Fig. 1. Analysis of crystalline phases formed in $2LiX-GaF_3$ (X = Cl, Br, I) via powder X-ray diffraction. (A) An overview of the pXRD patterns of $2LiX-GaF_3$ and GaF_3 . Identification of minor crystalline phases in (B) $2LiCl-GaF_3$, (C) $2LiBr-GaF_3$, and (D) $2LiI-GaF_3$, based on the ICSD database.

Ionic conductivities dependent on halide-anion species

The ionic conductivities of 2LiX-GaF_3 (X = Cl, Br, I) samples determined via variable-temperature electrochemical impedance spectroscopy (EIS) are shown in Figure 2. All samples exhibit a curvature in the $\log_{10}(\sigma)$ vs 1/T plot showing a deviation from the Arrhenius behavior. This deviation from Arrhenius behavior is typically observed in glass and polymer-based solid electrolytes. $^{25-27}$

Overall, at 25°C, 2LiCl-GaF₃ has the highest ionic conductivity of 3.2 mS/cm among the three. The ionic conductivity drops upon Cl⁻ substitution with Br⁻ (8.39 × 10⁻¹ mS/cm) and is the lowest with I⁻ (3.04 × 10⁻² mS/cm). The crystalline phases observed using X-ray diffraction (Figure 1) such as Li₃GaF₆ and LiGaX₄ have poor ionic conductivity.²⁸⁻³⁰ Therefore, the difference in ionic conductivities of 2LiX-GaF₃ (X=Cl, Br, I) implies that the presence of mixed-halide anion species affects the local structure and energy landscape for Li⁺-ion transport.

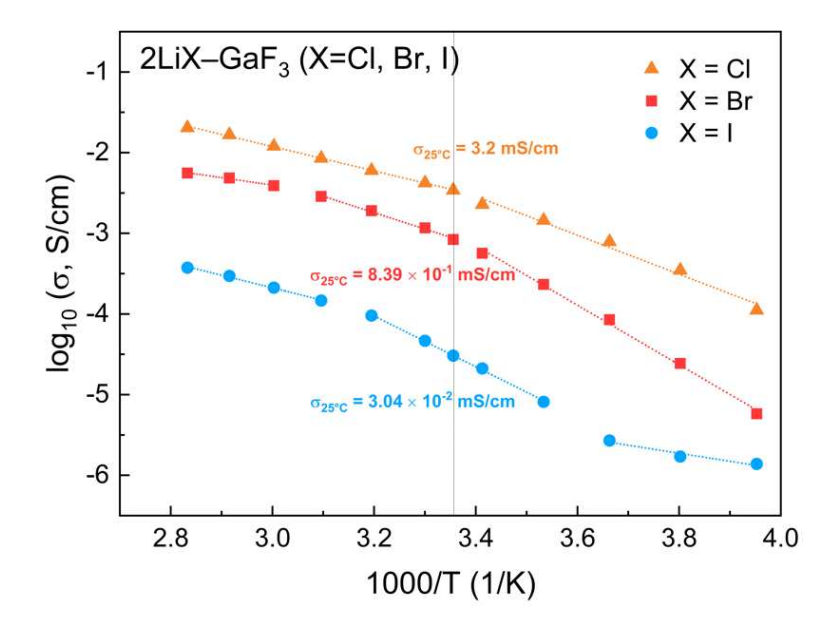


Fig. 2. Ionic conductivities of 2LiX-GaF₃ (X=Cl, Br, I) electrolytes. Measurements were determined using AC electrochemical impedance spectroscopy.

Local structures of 2LiX- GaF_3 (X = Cl, Br, I)

Solid-state NMR is a powerful tool for characterizing local structures of highly disordered materials. A combination of multinuclear ⁷¹Ga, ¹⁹F, and ⁷Li NMR, along with DFT-generated amorphous models, was used to investigate local structures in the 2LiX-GaF₃ compounds.

1) The gallium environment

High-resolution ⁷¹Ga NMR was collected to probe the local environment of Ga. ⁷¹Ga is an NMR-active quadrupole (spin-3/2) nucleus, therefore the electric field gradient around the Ga ions is highly sensitive to its local structural environment. To ensure broadband excitation, a Quadrupolar Carr-Purcell Meiboom-Gill (QCPMG) pulse sequence was employed to acquire ⁷¹Ga NMR spectra, which are shown in **Error! Reference source not found.**a. QCPMG NMR yields a series of evenly spaced spikelets, the skyline of which formulates the NMR peak shape.

The chemical shift of Ga in oxidation state +3 generally ranges from 700 to 0 ppm, whereas Ga in oxidation state +1 ranges from 0 to -700 ppm. $^{31-33}$ Since the 71 Ga peaks of 2LiX-GaF₃ (X = Cl, Br) spread through positive chemical shift ranges, we conclude that the majority of gallium in 2LiX-GaF₃ (X = Cl, Br) exists in oxidation state +3. In 2LiI-GaF₃, the 71 Ga NMR shows the largest bandwidth spanning from -250-300 ppm, which hints the existence of gallium in mixed oxidation states of +3, +2, and +1.

The broadening of the main 71 Ga NMR resonance (**Error! Reference source not found.a**) indicates that gallium exists in a disordered environment. The parameters used to fit these 71 Ga NMR resonances are presented in Table 1. A large quadrupole coupling constant (C_q) value of > 8 MHz is found. The Ga peak shifts towards lower ppm in 2LiX-GaF₃ from X = Cl to Br and I. This is in agreement with literature reports where Ga coordinated by I^- shows upfield shift compared to Ga coordinated by Cl^- and Br^- anions. $^{34-36}$ The different anion electronegativities may account for the differences in chemical shift. An additional small symmetric peak is observed around 40 ppm in the 2LiCl-GaF₃ phase. Such a peak is attributed to the crystalline Li_3GaF_6 phase which is also

Science Advances Manuscript Template Page 5 of 21

evident in powder X-ray diffraction (Error! Reference source not found.). The other crystalline phases identified from the XRD pattern, *i.e.*, LiGa X_4 (X = Cl, Br, I), may be hidden underneath the main broad 71 Ga band.

Further insight into the Ga coordination environment is provided by DFT simulations. An example of amorphous structure model obtained by *ab initio* molecular dynamics (AIMD) simulated annealing for 2LiCl-GaF₃ is presented in Error! Reference source not found.b. **Error!** Reference source not found.c illustrates the statistical distribution of X and F anions around Ga in the amorphous structure models generated for the different 2LiX-GaF₃ (X = Cl, Br, I) compositions. All structures contain mixed GaX_mF_{n-m} polyanions with the numbers m and (n-m) of X and F ligands being negatively correlated. Ga is found in highly diverse coordination environments. Ga^{3+} is coordinated by X and F anions in tetrahedral (IV, n = 4), pentahedral (V, n = 5), and octahedral (VI, n = 6) forms. Due to large quadrupolar couplings in all such environments, as expected from NMR data on reference Ga oxides (C_q up to ~17 MHz),³⁷ the resonance of Ga^{3+} in (IV) vs. (V) coordination is not distinguishable in the ⁷¹Ga NMR spectra, therefore Ga (IV) and (V) are referred to as a single complex anion.

 C_q and asymmetry parameters of Ga in the simulated 2LiX-GaF_3 (X = Cl, Br, I) amorphous structures were calculated by DFT NMR. The results are reported in Table 11 and in the supplementary Table S1. A large C_q of > 8 MHz is calculated for most Ga^{3+} Error! Reference source not found. Table 1. Comparisons between Ga coordination environments in the DFT simulated amorphous structures for 2LiCl-GaF_3 , 2LiBr-GaF_3 and 2LiI-GaF_3 Error! Reference source not found. 3c), also reveal a somewhat greater variety of mixed GaX_mF_{n-m} polyanions, in terms of the numbers m and (n-m) of X and F anions coordinating Ga, in the chlorine-based compound than in the bromine and iodine ones. That is, while in simulated 2LiCl-GaF_3 amorphous structures Ga shows a high likelihood of forming complex mixed GaX_mF_{n-m} polyanions with n=4,5,6 and m=1,2,3, a somewhat more homogeneous Ga coordination by X and F is found in the amorphous models of 2LiBr-GaF_3 ($n \approx 5$, $m \approx 2$), and of 2LiI-GaF_3 , where $n \approx 4$ and $m \approx 2-3$.

Some amorphous structure models are further characterized by the presence of direct Ga-Ga interactions (bond length $d_{\text{Ga-Ga}} \approx 2.45 \,\text{Å}$) forming dimeric $\text{Ga}_2(\text{X}, \text{F})_6$ units typical of Ga^{2+} compounds such as GaS (ICSD ID: 25660). In particular, $\text{Ga}_2(\text{X}, \text{F})_6$ dimers involve a significant amount (up to about 20%) of Ga atoms in 2LiI-GaF₃, whereas they only account for less than 10% of Ga in the other compositions. Finally, a small portion of Ga (~3%) in simulated amorphous 2LiI-GaF₃ is not covalently bonded into any molecular species, the distance from the nearest I⁻ and F⁻ anions ($d_{\text{Ga-I}} \approx 3.3 \,\text{Å}$, $d_{\text{Ga-F}} \approx 2.7 \,\text{Å}$) being far larger than the sum of the corresponding ionic radii (i.e., 2.8 Å and 1.9 Å, respectively), as shown by the pair distribution functions (PDFs) in Figure S1. Interaction distances $d_{\text{Ga-I}} > 3 \,\text{Å}$ are comparable to those occurring around Ga¹⁺ in GaI₂ (ICSD ID: 24821). Therefore, we assign formal oxidation state +1 to such non-covalently bonded Ga species. Indeed, the associated Bader charge is ~0.6 |e⁻|, much lower than the average Ga charge calculated for 2LiI-GaF₃, i.e., ~1.4 |e⁻|. It is noteworthy that the presence of Ga²⁺ and, albeit minor, of Ga¹⁺ in 2LiI-GaF₃ is consistent with both the significant broadening and upfield shift of the ⁷¹Ga NMR signal observed for 2LiI-GaF₃ (**Error! Reference source not found.**a).

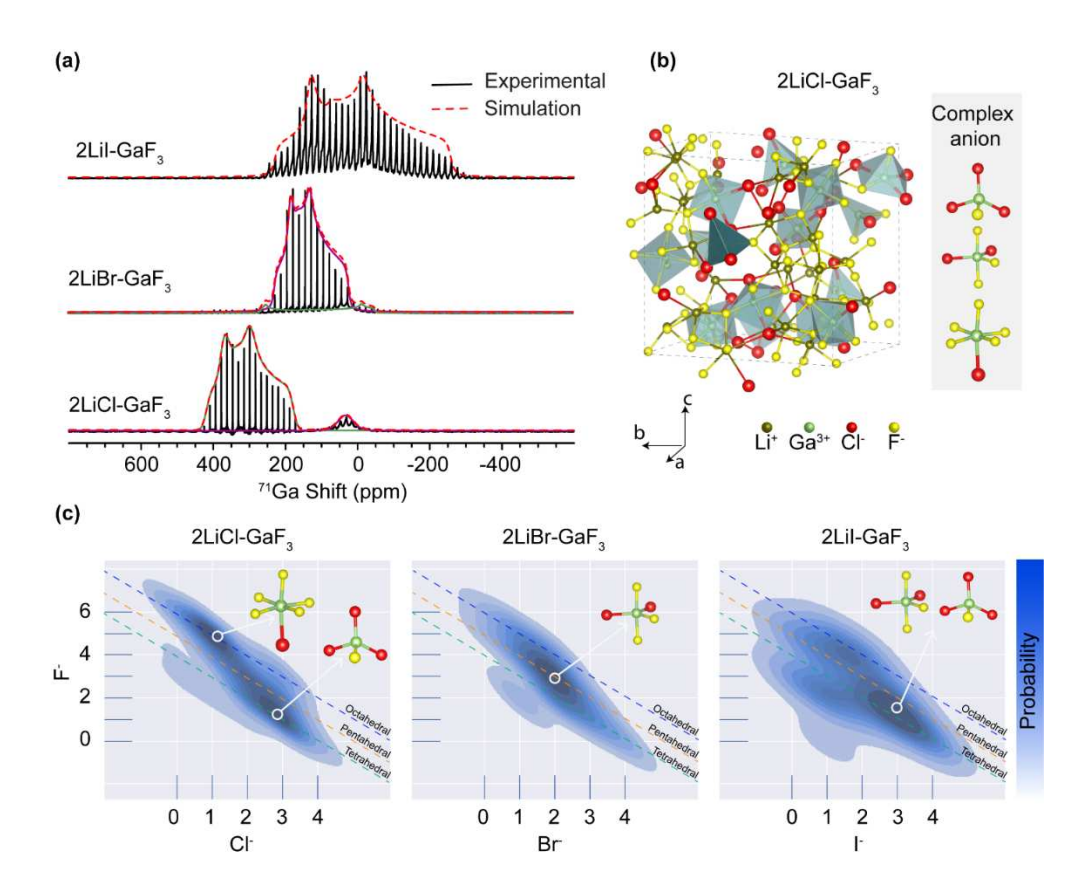


Fig. 3. Ga coordination environment examined with 71 Ga NMR and AIMD simulations. (A) Static QCPMG 71 Ga NMR spectra of 2LiX-GaF $_3$ (X = Cl, Br, I) and corresponding spectral fits. The resulting quadrupolar coupling constants and asymmetry parameters are documented in Table 1. (B) Simulated amorphous structure of 2LiCl-GaF $_3$ showing gallium coordinated with fluorine and chlorine to form complex anions $GaCl_mF_{n-m}$. (C) Statistical distribution of F and X anions coordinating Ga in the amorphous structural models for 2LiX-GaF $_3$, generated with AIMD simulated annealing. Among the most probable complex anions are $GaCl_1F_5$, $GaCl_3F_1$, $GaBr_2F_3$, and GaI_3F_1 .

Table 1 Quadrupole coupling constants C_q and η (asymmetry parameter) of ^{71}Ga NMR obtained for 2LiX-GaF₃ (X = Cl, Br, I) compounds both from experimental and computational methods. The computational Cq was derived by taking the average of the most common coordination types in 2LiCl-GaF₃, 2LiBr-GaF₃, and in 2LiI-GaF₃ in Table S1, as found from the X and F distributions shown in Error! Reference source not found.c.

Samples	Experimental C _q	ŋ	Computational C _q	ŋ
	(MHz)		(MHz)	
2LiCl-GaF ₃	8.8	0.61	12.6	0.7
2LiBr-GaF ₃	8.0	0.65	11.7	0.7
2LiI-GaF ₃	12.5	0.60	14.9	0.45

2) The fluorine environment

Further structural insights into 2LiX-GaF_3 (X = Cl, Br, I) are obtained by analyzing the local fluorine chemical environment using ¹⁹F NMR. Error! Reference source not found a shows the ¹⁹F NMR spectra. Solid GaF₃ (shown in blue at the top) resonates at -170 ppm with a shoulder to the

Science Advances Manuscript Template Page 7 of 21

left of the GaF_3 resonance that may be from the hydrated forms. ¹⁹F NMR of 2LiX- GaF_3 (X = Cl, Br, I) was performed under static conditions due to difficulties in spinning the samples.

 All spectra display multiple resonances signifying complex structural heterogeneity in the mixed-anion compounds. A broad peak is observed in all three samples, assigned to F coordinated in complex $Ga(X, F)_n$ polyanion species, *i.e.*, clustered F-, as shown in Error! Reference source not found.b. In agreement with the experimental observation, Error! Reference source not found.b shows that DFT-computed ¹⁹F chemical shifts for the amorphous model structure of 2LiCl- GaF_3 yield a similar broad peak spanning between -75 and -250 ppm. While this chemical shift range covers most of the experimental ¹⁹F NMR resonances, we notice that a small portion (less than 10% of the overall intensity) of the measured spectra extends further to 0 ppm. Such a discrepancy may be explained by the limited size and statistical representativity of our model, as well as by the absence, from the simulations, of broadening factors common to experimental NMR, such as thermal effects, orientation anisotropy in sample powders, and dipolar couplings, *etc*.

Quantification of the resonances from ¹⁹F NMR is presented in Error! Reference source not found.c. Upon replacement of Cl⁻ with Br⁻ and with I⁻, the intensity of the complex anion resonance decreases, whereas a new sharp resonance appears at ≈ -129 to -133 ppm in the 2LiBr-GaF₃ and 2LiI-GaF₃ samples, respectively. The sharp resonance is attributed to single "mobile" F⁻ anions. Since the NMR spectra were collected under static conditions, homonuclear dipolar interactions dominate the line broadening in ¹⁹F NMR. Therefore, a narrow line shape is indicative of weaker dipolar interactions which may be related to F⁻ species with high mobility. Indeed, a survey of ¹⁹F-NMR data on F⁻-ion conductors demonstrates resemblance in line shape width (< 1 kHz). ³⁸⁻⁴⁰ Therefore, the overall ionic conductivities measured for 2LiBr-GaF₃ and 2LiI-GaF₃ may contain contributions from both Li⁺ and F⁻ ion transport. The Li⁺ conduction in 2LiBr-GaF₃ and 2LiI-GaF₃ may be even more strongly hindered than the apparent ionic conductivities suggest.

Residual sharp peaks, which we label as "unknown" species in Error! Reference source not found.c, may possibly be attributed to the minor crystal phases that matched in powder XRD (Error! Reference source not found.). In the case of 2LiCl-GaF₃, crystalline Li₃GaF₆ is a probable phase at -161 ppm. In the case of 2LiBr-GaF₃ and 2LiI-GaF₃,the "unknown" peaks reside at -129 ppm. Those peaks remain unassigned, but we hypothesize contributions from mono-anion species similar to HF, the chemical shift of which varies between -140 and -160 ppm. 41

Science Advances Manuscript Template Page 8 of 21

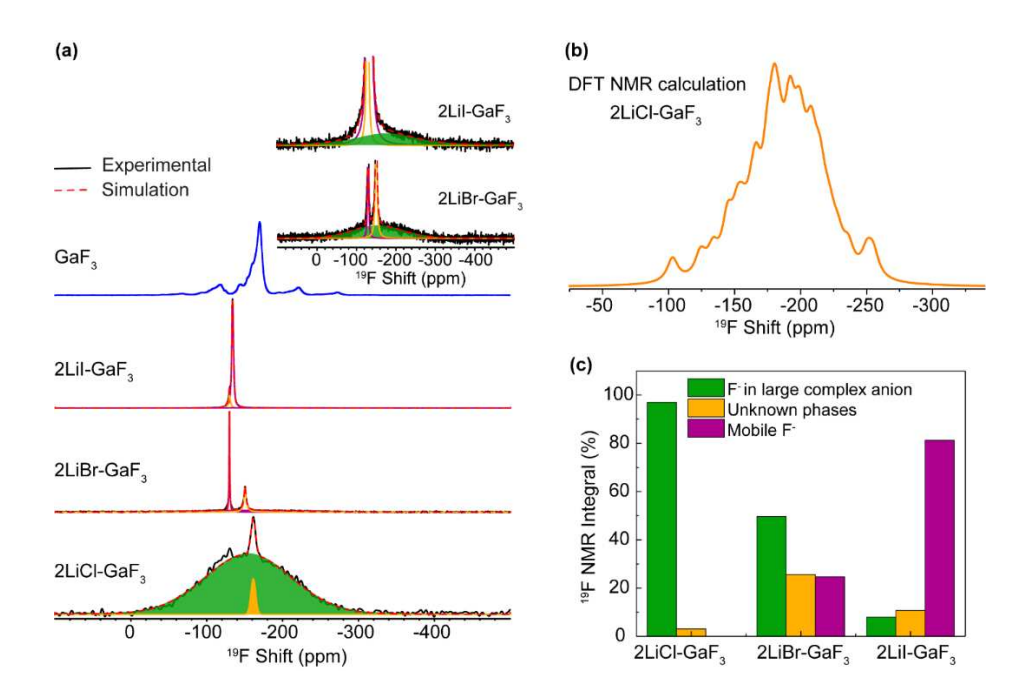


Fig. 4. Quantification of F⁻ integrated into complex GaX_mF_{n-m} anions in $2LiX-GaF_3$ (X = Cl, Br, I) with ¹⁹F NMR. (A) Static ¹⁹F NMR spectra of $2LiX-GaF_3$ (X = Cl, Br, I). The broad Gaussian peak comes from complex GaX_mF_{n-m} anions with limited mobility. The sharp NMR resonances are from highly mobile F⁻ ions. (B) DFT calculated ¹⁹F NMR based on the amorphous structure model for $2LiCl-GaF_3$ as shown in Error! Reference source not found.b. (C) Quantification of F in different chemical environments based on ¹⁹F NMR in (A).

3) The lithium environment

Additionally, ⁷Li NMR was employed to probe the Li⁺-ion environment. In all three compositions, a broad and a narrow resonance of ⁷Li are observed, as shown in Fig. 1a. The sharp Lorentzian peak shape is typical of Li ions in fast ion conductors, whereas the broad Gaussian peak shape often represents Li ions with low mobility in anisotropic environments. ^{42, 43} Therefore, we attribute the broad resonance to a slow-moving Li component and the sharp resonance to a fast-moving Li component. Quantification of the broad and sharp components in the three compositions is presented in Fig. 1b: the composition 2LiCl-GaF₃ displays the largest fraction of fast-moving Li⁺, in agreement with it having the highest measured ionic conductivity.

Fig. 1c provides a statistical analysis of the Li⁺ environments observed in the amorphous structure models generated with AIMD-simulated annealing for 2LiX-GaF_3 (X = Cl, Br, I). We notice that for X=Cl, the Li⁺ coordination environment is somewhat diversified, including both tetrahedral and pentahedral local structures, whereas for X=Br, I, the Li⁺ is found mainly in tetrahedral coordination. Furthermore, the affinity of the X anions towards Li⁺ decreases from X = Cl⁻, to Br⁻, and to I⁻. Indeed, as indicated by the maxima in the probability distribution highlighted in Fig. 1c, the average number of X⁻ anions around Li⁺ diminishes from being approximately 2 for X = Cl, to 0-1 for X = Br and to 0 for X = I, while the relative amount of F⁻ increases. In drawing a parallel with the two Li⁺ components detected in the ⁷Fig. 14a), we might associate the broad peak that prevails in 2LiI-GaF_3 to Li⁺-ions mainly involved in strong interactions with the highly electronegative F⁻, whereas the sharp Lorentzian peak of the fast-moving Li component, that is most abundant in 2LiCl-GaF_3 , might be attributed to Li⁺-ions contended with $\text{GaX}_m\text{F}_{\text{n-m}}$ (n-m > 0, m > 0) polyanions.

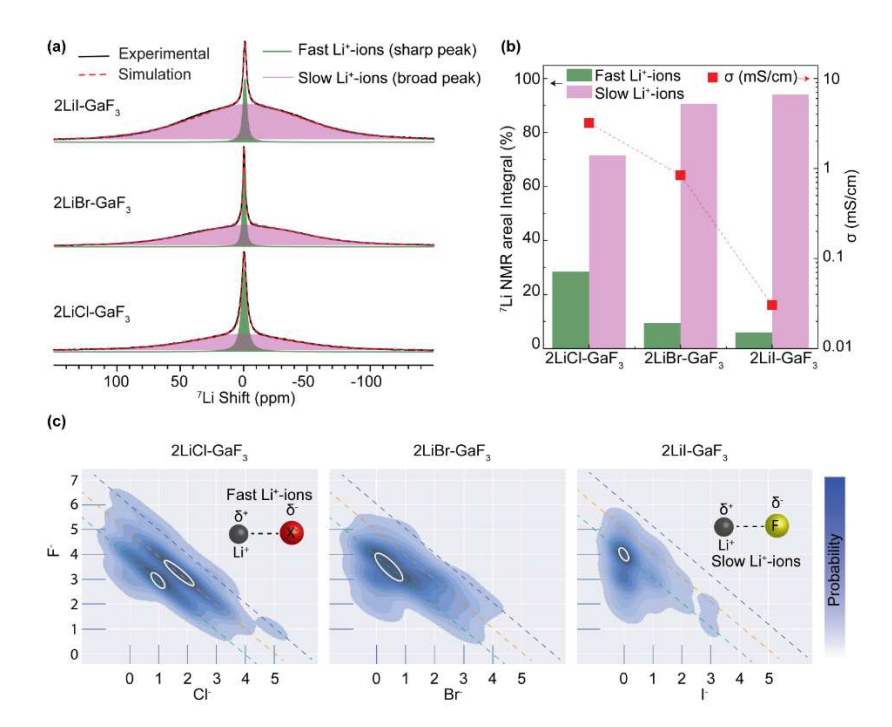


Fig. 1. Analysis of Li local environments in 2LiX-GaF₃ (X = Cl, Br, I) with ⁷Li NMR and AIMD simulations. (A) ⁷Li NMR spectra of 2LiX-GaF₃ exhibit two resonances: the sharp one comes from fast-moving Li⁺-ions and the broad one is from slow-moving Li⁺-ions. Li⁺-ion dynamics are determined with NMR relaxometry shown in Fig. 6. (B) Quantification of the slow- and fast-moving Li⁺-ions based on ⁷Li NMR in (A). (C) Analysis of Li⁺ coordination by F⁻ and X⁻ anions in the amorphous structure models for 2LiX-GaF₃ generated with AIMD simulated annealing.

Li-ion dynamics in 2LiX-GaF₃ (X = Cl, Br, I)

Multinuclear solid-state NMR reveals that LiX and GaF₃ react to form complex mixed anions of Ga(F, X)_n. To understand the impact of this polyanion-constituted framework on the Li⁺ dynamics, ⁷Li NMR relaxometry is employed. ⁷Li T₁ relaxation time is known to be correlated with the Li⁺-ion motional rate (1/ τ_c), according to equation (1)^{44,45} where γ is the gyromagnetic ratio, μ_o is permeability of vacuum, \hbar is the reduced Planck constant, r_o is the interatomic distance, and ω_o is the Larmor frequency.

$$\left(\frac{1}{T_1}\right) = \frac{3\mu_0^2 \gamma^4 \hbar^2}{10r_0^6} \left[\frac{\tau_c}{1 + (\omega_0 \tau_c)^2} + \frac{4\tau_c}{1 + 4(\omega_0 \tau_c)^2} \right]$$
(1)

Two motional regimes are depicted from equation (1), the fast-motional regime where $\omega_o \tau_c << 1$ and slow-motional regime where $\omega_o \tau_c >> 1$. To determine the motional regime of Li⁺ ions, variable-temperature NMR relaxometry studies were conducted on the highly conductive 2LiCl-GaF₃ sample. **Error! Reference source not found.** a shows the ⁷Li NMR spectra collected at temperatures between 25 and 95 °C. While the resonances of the fast- and slow-moving Li components are both observed throughout the explored temperature range, increasing the temperature from 20 to 95 °C involves converting slow-moving Li⁺ ions to fast-moving ones. The quantification of the NMR resonances is presented in **Error! Reference source not found.** b. We observe a progressive increase of the fraction of the fast-moving Li⁺ ions at the cost of the slow-moving ones, which plateaus at T = 70 °C, suggesting an increase in the charge carrier concentration.

Science Advances Manuscript Template Page 10 of 21

From variable-temperature T_1 relaxation measurements (Error! Reference source not found.c), we also observe that the increase in temperature does not cause significant changes in the T_1 relaxation of the resonance attributed to fast Li^+ ions, whereas the relaxation time of the resonance from the slow Li^+ ions decreases from 1.55 sec at 25 °C to 1.06 sec 95 °C. This indicates that the two phases may be at different motional regimes of the Bloembergen-Purcell-Pound (BPP) theory. The slow Li^+ ions are in the slow motional regime where $\omega_o \tau_c >> 1$, and shorter T_1 relaxation time depicts faster motion. The initial abnormal behavior of the T_1 of slow Li^+ ions is likely due to phase transition below 40°C, echoing the electrochemical measurements shown in Figure 2. The NMR resonance from the fast Li^+ ions does not show significant changes in the T_1 relaxation time, suggesting that the motion of these Li^+ ions lie in the intermediate region where $\omega_o \tau_c \approx 1$. High ionic conductivity at high temperature is attributed to the increased fraction of the fast Li^+ -ion component (shorter T_1 relaxation time), *i.e.*, increase in charge carrier concentration, as shown in Figure 6c.

Science Advances Manuscript Template Page 11 of 21

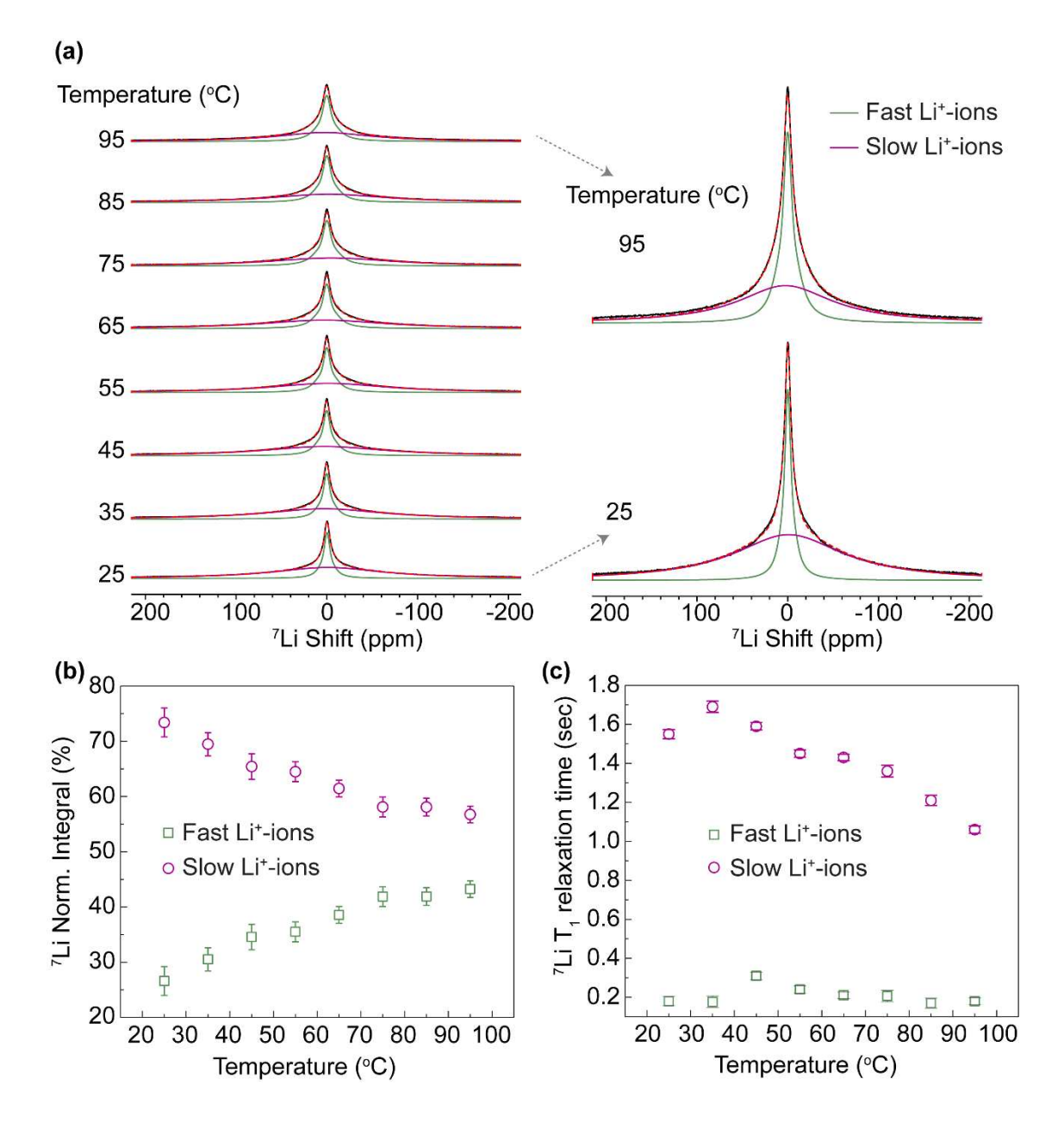


Fig. 6. Li⁺-ion dynamics of 2LiCl-GaF₃ probed with variable-temperature NMR lineshape analysis and relaxometry. (A) Variable-temperature static ⁷Li NMR spectra, revealing that the resonances of the fast-moving and slow-moving Li⁺-ions adopt Lorentzian and Gaussian peak shapes, respectively. The Lorentzian line shape suggests fast relaxation induced by ion dynamics. (B) The quantified fractions of the fast- and slow-moving Li⁺-ions as a function of temperature obtained from the analysis of variable-temperature spectra in (a). (C) ⁷Li NMR T₁ relaxation time measurements of 2LiCl-GaF₃ as a function of temperature.

Further insights into the impact of the anion sub-lattice on the Li⁺-ion dynamics can be obtained by comparing room-temperature 7 Li T_1 NMR relaxation times of 2 LiX-GaF₃ (X = Cl, Br, I). Error! Reference source not found. shows the 7 Li T_1 relaxation times of the broad and sharp components in 7 Li NMR spectra of 2 LiX-GaF₃ (X = Cl, Br, I). The fast-moving component is associated with a shorter T_1 relaxation time than the slow-moving component in all samples. 2 LiCl-GaF₃ has the

Science Advances

Manuscript Template

Page 12 of 21



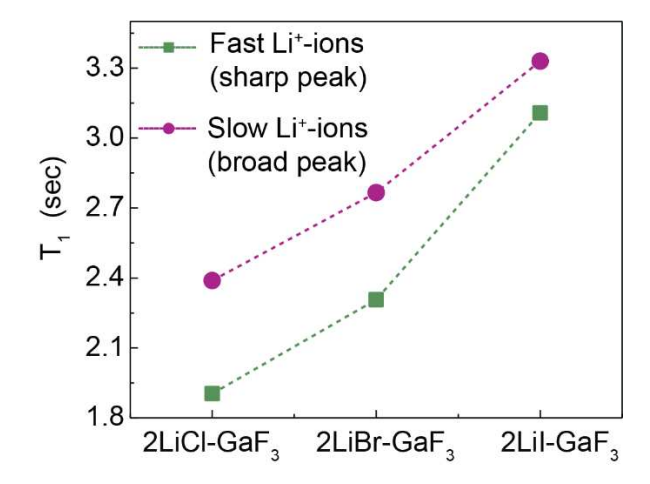


Fig. 7. Li⁺-ion dynamics of 2LiX-GaF₃ (X=Cl, Br, I) probed with NMR relaxometry. Room-temperature 7 Li NMR T₁ relaxation times of the slow and fast-moving components in 2LiX-GaF₃ (X = Cl, Br, I).

Discussion

Amorphous 2LiX-GaF_3 (X = Cl, Br, I) compounds are pliable fast Li⁺ conductors, with ionic conductivities increasing from 3.3×10^{-2} mS/cm for 2LiI-GaF_3 , to 0.84 mS/cm for 2LiBr-GaF_3 , and up to 3.2 mS/cm for 2LiCl-GaF_3 . In this work, we have combined multi-nuclear solid-state NMR and DFT to characterize local structures and ion dynamics in these complex mixed-halide materials to understand the impact of composition on ionic conductivity.

found.a) reveal that Ga is mostly 3+. Moreover, the large C_q constant (> 8 MHz) values indicate local disorder, which we ascribe to the existence of a wide variety of coordination environments around Ga, with coordination numbers ranging from n=4 to n=6. Indeed, AIMD-generated amorphous structure models (Error! Reference source not found.b-c) display considerable statistical variance in the Ga coordination of polyhedra GaX_mF_{n-m} formed during the simulated annealing process. Interestingly, while the X halides Br^- and I^- form essentially one main type of GaX_mF_{n-m} polyanion, with $n \approx 5$ ($m \approx 2$) and $n \approx 4$ ($m \approx 2$ -3), respectively, the chlorine-based compound is characterized by a multimodal distribution of Ga environments, with local maxima at $n \approx 4$ ($m \approx 3$), $n \approx 5$ ($m \approx 2$) and $n \approx 6$ ($m \approx 1$), see Error! Reference source not found.c. We also note that, despite the wide dispersion of the DFT calculated C_q values, C_q^{DFT} (Table S1), average \bar{C}_q^{DFT} calculated for GaX_mF_{n-m} polyanions corresponding to the maxima outlined above are very close to the C_q values used for the experimental fitting (Table 1), namely, $\bar{C}_q^{DFT} = 12.6$ MHz (n = 4, 5, 6; m = 1, 2, 3) for 2LiCl-GaF3; $\bar{C}_q^{DFT} = 11.7$ MHz (n = 5; m = 2) for 2LiBr-GaF3; and $\bar{C}_q^{DFT} = 14.9$ MHz (n = 4; m = 2-3) for 2LiI-GaF3.

The greater coordination flexibility of Ga in 2LiCl-GaF₃ may be attributed to two main factors. First, Cl⁻ has a smaller ionic radius (1.81 Å) than Br⁻ (1.96 Å) and I⁻ (2.2 Å), which leaves room for

Science Advances Manuscript Template Page 13 of 21

a relatively larger number of both Cl⁻ and F⁻ ligands around Ga. Second, the electronegativity of Cl (3.16) is closer to that of F (3.98), which allows for a more homogeneous distribution of the electron density in mixed $Ga(Cl, F)_n$ polyanions and, therefore, for greater stability over a wide coordination range (n = 4, 5, 6), as demonstrated by the defect energies reported in Table S2.

The complex $Ga(X, F)_n$ polyanions are further studied by examining the fluorine environment. Based on our DFT structure models, $Ga(X, F)_n$ polyanions are formed by partial substitution of F with X in the octahedral $[GaF_6]^{3-}$ building blocks of the GaF_3 precursor. **Error! Reference source not found.**c shows that, in general, F is displaced from its original position relative to Ga to a greater extent when bigger X halides ($I^- > Br^- > Cl^-$) are introduced. As fluorine is detached from its polar-covalent interaction with Ga, free F^- anions are released into the amorphous matrix. Hence, two different types of fluorine are outlined, namely, (i) F covalently bound to Ga in mixed polyanions $Ga(X, F)_n$, and (ii) free F^- anions with high mobility, as observed in ^{19}F NMR (**Error! Reference source not found.**a-c). Single F^- anions are expected to have higher mobility compared to relatively large polyanions such as $Ga(X, F)_n$. Moreover, the increasing intensity of the ^{19}F NMR narrow peak (FWHM < 1 kHz) from fast-moving F^- anions in the 2LiBr-GaF3 and 2LiI-GaF3 samples, correlates with the increasing amount of free F^- in the corresponding structural models, thus supporting this interpretation. The ^{19}F NMR signals integration in **Error! Reference source not found.**c, reveals that more than 80% of F in 2LiI-GaF3 is mobile and does not participate in the formation of $Ga(X, F)_n$ polyanions.

In contrast to the increasing amount of fast-moving F observed in ¹⁹F NMR, ⁷Li NMR reveals that the amount of mobile Li decreases with X varying from Cl to Br and I. The sharp ⁷Li NMR signal from fast-moving Li ions in 2LiI-GaF₃ is reduced to about 1/3 of that observed in 2LiCl-GaF₃ (Fig. 1a-b). This demonstrates that the formation of complex Ga(X, F)_n polyanions has a significant impact on the lithium chemical environment and, consequently, on the Li⁺ mobility. Once again, further insight can be achieved by inspecting the Li(X, F) local structures formed in the amorphous models generated by simulated annealing. In this case, a clear correspondence emerges between the intensification of the ⁷Li NMR signal from slow-moving Li (and parallel decrease of the fast-moving Li component) observed as X changes from Cl to Br and to I, and the prevalence of F⁻ (over Ga(X, F)_n polyanions) as the counter-ion around Li⁺. It is noteworthy that the Li⁺ environment is ultimately shaped by the variety of mixed-halide polyanions formed around Ga, which drive the short-range ordering constituting the amorphous framework of 2LiX-GaF₃ compounds.

Variable-temperature ⁷Li NMR of 2LiCl-GaF₃ deciphers the transition of slow-moving Li to the fast-moving Li phase as shown in Figure 6b. We thereby conclude that the more Li⁺ is engaged in strong ionic interactions with highly electronegative free F⁻ anions, the more the Li⁺ mobility in 2LiX-GaF₃ compounds is hindered. This feature finally explains the lower ionic conductivity of the 2LiBr-GaF₃ and 2LiI-GaF₃ compounds compared to 2LiCl-GaF₃. The involvement of fluorine in the constitutive polyanionic framework of the latter limits the binding effect of F⁻ anions on the charge carriers, thus providing Li⁺ with more freedom to diffuse through the amorphous medium.

The present work elucidates local structures in amorphous 2LiX-GaF_3 (X = Cl, Br, I) electrolytes and determines the origin of high ionic conductivity via a combined approach of advanced solid-state NMR characterizations and DFT calculations. High-energy mechanochemical mixing of binary lithium halides LiX with GaF₃ results in the formation of complex anions $\text{Ga}(X, F)_n$. A larger variety of $\text{GaX}_m F_{n-m}$ coordination polyhedra are formed in accommodating X = Cl along with F, as opposed to X = Br or I. The F involvement in forming $\text{GaX}_m F_{n-m}$ polyanions is beneficial for fast Li⁺ ion conduction due to consequent diversification of the Li environment avoiding exclusive Li-F ionic interactions. The clustering of the halides on gallium-based polyanions weakens the Li⁺ binding affinity of the negative host enabling fast ion transport.

Science Advances Manuscript Template Page 14 of 21

This study introduces a novel concept of charge clustering for electrolyte design, broadly relevant to liquid-, polymer-, and ceramic/glass-type ion conductors. Therefore, we expect this work will inspire new frontiers for electrolyte research beyond utilizing simple anions or polyanions, which could potentially produce electrolytes with performance far exceeding state-of-the-art. Specifically, in the case of amorphous 2LiX-GaF₃ electrolytes, this strategy also affords the employment of halide elements to enhance the electrochemical stability without introducing strong Li-halide interactions. Finally, we note that the phenomenon of charge-clustering on Ga(X,F)n polyanions to weaken cation binding is analogous to a phenomenon recently observed in biological systems, *i.e.*, clustering of carboxylate (COO⁻) groups on proteins which significantly alters their binding to Ca²⁺ and Mg²⁺. Therefore, our findings may also help to design multi-valent (Ca²⁺ and Mg²⁺) ion conductors, a currently challenging area of research, and will generate broader and high impacts if successful.

Materials and Methods

Synthesis of 2LiX–GaF₃ (X=Cl, Br, I) - The materials were prepared by planetary milling (Pulverisette 7 PL; Fritsch) using as-received LiCl (99 %; Sigma-Aldrich), LiBr (≥99 %; Sigma-Aldrich), LiI (99.9 %; Sigma-Aldrich), and GaF₃ (99.85 %; Alfa-Aesar) in the same way as described in our previous work.²³ LiX/GaF₃ (2/1, mol/mol) were placed into a silicon nitride container which was sealed in an Ar-filled glove box to minimize air exposure during the mechanochemical synthesis. The powders were mixed at 700 rpm for 10 min, followed by 5 min rest, and this mixing and rest procedure was repeated 72 times, resulting in a clay-like compound.

X-ray Diffraction – "Clay-like" samples were packed in a zero-background XRD sample holder which was covered with a polyimide Kapton film to minimize sample exposure to humid air. XRD was performed using a Rigaku D8 powder diffractometer with the Bragg-Brentano geometry at a voltage of 44 kV and a current of 40 mA with Cu-K α radiation (λ = 1.5406 Å). The data was collected in the 2 Θ range of 10°-80° at a step size of 0.03° with a total acquisition time of 30 minutes.

Electrochemical analysis – The ionic conductivity was determined using electrochemical impedance spectroscopy (EIS, Solartron Analytical, UK). EIS was performed using the cell confirmation of stainless steel/2LiX–GaF₃/stainless steel in the frequency range from 1 MHz to 0.1 Hz and a temperature range of 20 –80 °C.

Solid-state NMR - ⁷Li (spin-3/2) and ¹⁹F (spin-1/2) solid-state NMR experiments were performed using a Bruker Avance-III 500 MHz (11.7 T) spectrometer at Larmor frequencies of 194.4 MHz and 470 MHz, respectively. Experiments were carried out under static conditions, as the "clay-like" nature of the samples made them unsuitable for magic-angle-spinning (MAS) NMR experiments. Single-pulse ⁷Li NMR experiments were performed with a $\pi/2$ pulse length of 3.1 µs and a recycle delay of 20 s. For 19 F NMR, a static spin-echo sequence was employed with a $\pi/2$ pulse length of 4.4 µs and a recycle delay of 50 s. ⁷¹Ga (spin-3/2) NMR was performed on an 830 MHz (19.6 T) spectrometer at the Larmor frequency of 253 MHz. A static quadrupolar Carr-Purcell-Meiboom-Gil (QCPMG) pulse sequence with a $\pi/2$ pulse length of 2 µs was used to acquire the ⁷¹Ga NMR spectra. Variable-temperature ⁷Li NMR spectroscopy and relaxometry measurements on 2LiCl-GaF₃ were conducted to determine Li⁺-ion dynamics using a Bruker 300 MHz (7.05 T) spectrometer at the Larmor frequency of 116 MHz, and a 4-mm Bruker MAS NMR probe at an 8-kHz spinning rate. The inversion recovery pulse sequence was used to determine ⁷Li T_1 relaxation times, with a $\pi/2$ pulse length of 2.5 µs. The spectra were collected between 25-95 °C with increments of every 10 °C and the sample was allowed to equilibrate for 10 minutes at each temperature. All ⁷Li spectra were calibrated using LiCl(s) at -1.1 ppm and ¹⁹F NMR using LiF(s) at -203 ppm. ⁷¹Ga NMR was calibrated using GaF₃(s) at 0 ppm.

Computational

45

46

47

48

49

50

51

52

53

54

55

56

57

58

59

60

61

62

63

64

65

66

67

68

69

70

71

72

73 74

75

76 77

78

79

80

81

82 83

84

85

86

87

88

89

Simulated annealing – Amorphous 2LiX-GaF₃ (X = Cl, Br, and I) structure models were generated via ab initio molecular dynamics (AIMD) simulated annealing followed by structure relaxation performed with the Vienna Ab initio Simulation Package (Vasp). 46 Projector-augmented wave potentials were used within the generalized gradient approximation of the density functional in its Perdew-Burke-Ernzerhof formulation. 47,48 AIMD simulations were carried out at the Γ-point only, using the largest default kinetic energy cutoff of constituent elements. The AIMD time step was set to 1-2 fs, and the temperature was controlled by periodic velocity rescaling every 50 or 100 steps. Following Refs.^{49,50} initial atomic configurations were built in cubic volumes using the packing optimization procedure developed in Packmol.⁵¹ These atomic configurations were used as high-temperature (1000-2000K) structure guesses to which a descending temperature ramp was applied at a cooling rate of 100K/ps, discontinued by equilibration steps of at least 10 ps. All AIMD simulations were performed at constant volume, and the latter was resized isotropically (i.e., by variations of ± 0.1 Å along each Cartesian direction) at intervals during the equilibration to counterbalance the calculated total pressure. Structure optimizations following the cooling process were performed using the higher-accuracy DFT settings of the Materials Project.⁵² Atomic charges were calculated using Henkelman et al.'s algorithm for Bader decomposition of charge density.^{53,54} Local structures and coordination environments were analyzed using the CrystalNN near-neighbor finding algorithm implemented in the python library pymatgen. 55,56

NMR calculations – The optimized amorphous structures generated by simulated annealing were used for calculations of NMR tensors using the Gauge Including Projector Augmented Waves (GIPAW) method. 9,11 The energy cutoff was set to 600 eV and a k-point grid density of at least 500 per reciprocal atom (pra) was guaranteed. A threshold for convergence on the electronic energy of 10^{-8} eV was used to ensure high accuracy. Calibration factors (+ 90 ppm for 71 Ga shifts and +15 ppm for 19 F shifts 11) were obtained based on calculated and experimental shifts of model compounds GaF_3 . Electric field gradient (EFG) tensors were calculated to determine the quadrupole coupling constant (C_q). 12 The nuclear quadrupole moment (Q) of 71 Ga was set to 107 mb for the calculation of C_q . 14

References

- (1) Janek, J.; Zeier, W. G. A Solid Future for Battery Development. *Nature Energy* **2016**, *1* (9), 16141. https://doi.org/10.1038/nenergy.2016.141.
- (2) Manthiram, A.; Yu, X.; Wang, S. Lithium Battery Chemistries Enabled by Solid-State Electrolytes. *Nature Reviews Materials* **2017**, 2 (4), 16103. https://doi.org/10.1038/natrevmats.2016.103.
- (3) Abakumov, A. M.; Fedotov, S. S.; Antipov, E. V.; Tarascon, J.-M. Solid State Chemistry for Developing Better Metal-Ion Batteries. *Nature Communications* **2020**, *11* (1), 4976. https://doi.org/10.1038/s41467-020-18736-7.
- (4) Bachman, J. C.; Muy, S.; Grimaud, A.; Chang, H.-H.; Pour, N.; Lux, S. F.; Paschos, O.; Maglia, F.; Lupart, S.; Lamp, P.; Giordano, L.; Shao-Horn, Y. Inorganic Solid-State Electrolytes for Lithium Batteries: Mechanisms and Properties Governing Ion Conduction. *Chem. Rev.* **2016**, *116* (1), 140–162. https://doi.org/10.1021/acs.chemrev.5b00563.
- (5) Kato, Y.; Hori, S.; Saito, T.; Suzuki, K.; Hirayama, M.; Mitsui, A.; Yonemura, M.; Iba, H.; Kanno, R. High-Power All-Solid-State Batteries Using Sulfide Superionic Conductors. *Nature Energy* **2016**, *1*, 16030.
- 90 (6) Adeli, P.; Bazak, J. D.; Park, K. H.; Kochetkov, I.; Huq, A.; Goward, G. R.; Nazar, L. F. Boosting Solid-State Diffusivity and Conductivity in Lithium Superionic Argyrodites by Halide Substitution. *Angewandte Chemie International Edition* **2019**, *58* (26), 8681–8686. https://doi.org/10.1002/anie.201814222.

- 94 (7) Patel, S. V.; Banerjee, S.; Liu, H.; Wang, P.; Chien, P.-H.; Feng, X.; Liu, J.; Ong, S. P.; Hu, Y.-Y. Tunable Lithium-Ion Transport in Mixed-Halide Argyrodites Li6-XPS5-XClBrx: An 95 Compositional Space. Chem. Mater. 2021, 33 (4),1435–1443. 96 97 https://doi.org/10.1021/acs.chemmater.0c04650.
- Kraft, M. A.; Ohno, S.; Zinkevich, T.; Koerver, R.; Culver, S. P.; Fuchs, T.; Senyshyn, A.; 98 (8) 99 Indris, S.; Morgan, B. J.; Zeier, W. G. Inducing High Ionic Conductivity in the Lithium Superionic Argyrodites Li6+xP1-XGexS5I for All-Solid-State Batteries. J. Am. Chem. Soc. 00 01 **2018**, 140 (47), 16330–16339. https://doi.org/10.1021/jacs.8b10282.
- (9) Feng, X.; Chien, P.-H.; Wang, Y.; Patel, S.; Wang, P.; Liu, H.; Immediato-Scuotto, M.; Hu, 02 03 Y.-Y. Enhanced Ion Conduction by Enforcing Structural Disorder in Li-Deficient 04 Argyrodites Li6-xPS5-xCl1+x. Energy Storage Materials **2020**, *30*, 67–73. https://doi.org/10.1016/j.ensm.2020.04.042. 05
- Wang, P.; Patel, S.; Liu, H.; Chien, P.-H.; Feng, X.; Gao, L.; Chen, B.; Liu, J.; Hu, Y.-Y. (10)06 Configurational and Dynamical Heterogeneity in Superionic Li_{5.3}PS_{4.3}Cl_{1.7-x}Br_x. Advanced Functional Materials 2023, 2307954. https://doi.org/10.1002/adfm.202307954.

08

- Nazar, L.; Adeli, P.; Bazak, J. D.; Park, K.-H.; Kochetkov, I.; Huq, A.; Goward, G. Boosting 09 Solid-State Diffusivity and Conductivity in Lithium Superionic Argyrodites by Halide 10 Substitution. Angewandte Chemie International Edition 11 (ja). https://doi.org/10.1002/anie.201814222. 12
- Murugan, R.; Thangadurai, V.; Weppner, W. Fast Lithium Ion Conduction in Garnet-Type 13 14 Li7La3Zr2O12. Angewandte Chemie International Edition 2007, 46 (41), 7778–7781. https://doi.org/10.1002/anie.200701144. 15
- Wu, E. A.; Banerjee, S.; Tang, H.; Richardson, P. M.; Doux, J.-M.; Qi, J.; Zhu, Z.; Grenier, 16 17 A.; Li, Y.; Zhao, E.; Deysher, G.; Sebti, E.; Nguyen, H.; Stephens, R.; Verbist, G.; Chapman, K. W.; Clément, R. J.; Banerjee, A.; Meng, Y. S.; Ong, S. P. A Stable Cathode-Solid 18 19 Electrolyte Composite for High-Voltage, Long-Cycle-Life Solid-State Sodium-Ion Batteries. Nature Communications **2021**, 12 (1), 1256. https://doi.org/10.1038/s41467-021-21488-7. 20
- Xiao, Y.; Wang, Y.; Bo, S.-H.; Kim, J. C.; Miara, L. J.; Ceder, G. Understanding Interface 21 22 Stability in Solid-State Batteries. *Nature Reviews Materials* **2020**, 5 (2), 105–126. https://doi.org/10.1038/s41578-019-0157-5. 23
- 24 Banerjee, A.; Wang, X.; Fang, C.; Wu, E. A.; Meng, Y. S. Interfaces and Interphases in All-Solid-State Batteries with Inorganic Solid Electrolytes. Chem. Rev. 2020, 120 (14), 6878-25 6933. https://doi.org/10.1021/acs.chemrev.0c00101. 26
- Ding, Z.; Li, J.; Li, J.; An, C. Review—Interfaces: Key Issue to Be Solved for All Solid-27 State Lithium Battery Technologies. Journal of The Electrochemical Society 2020, 167 (7), 28 070541. https://doi.org/10.1149/1945-7111/ab7f84. 29
- 30 Huo, H.; Gao, J.; Zhao, N.; Zhang, D.; Holmes, N. G.; Li, X.; Sun, Y.; Fu, J.; Li, R.; Guo, X.; Sun, X. A Flexible Electron-Blocking Interfacial Shield for Dendrite-Free Solid Lithium 31 Metal Batteries. Nature Communications 2021, 12 (1), 176. https://doi.org/10.1038/s41467-32 020-20463-y. 33
- Cronau, M.; Szabo, M.; König, C.; Wassermann, T. B.; Roling, B. How to Measure a 34 Reliable Ionic Conductivity? The Stack Pressure Dilemma of Microcrystalline Sulfide-Based 35 Solid Electrolytes. ACS Lett. 2021, (9),3072-3077. Energy 36 37 https://doi.org/10.1021/acsenergylett.1c01299.
- Doux, J.-M.; Yang, Y.; Tan, D. H. S.; Nguyen, H.; Wu, E. A.; Wang, X.; Banerjee, A.; Meng, 38 Y. S. Pressure Effects on Sulfide Electrolytes for All Solid-State Batteries. J. Mater. Chem. 39 40 A 2020, 8 (10), 5049–5055. https://doi.org/10.1039/C9TA12889A.
- Minnmann, P.; Strauss, F.; Bielefeld, A.; Ruess, R.; Adelhelm, P.; Burkhardt, S.; Dreyer, S. 41 L.; Trevisanello, E.; Ehrenberg, H.; Brezesinski, T.; Richter, F. H.; Janek, J. Designing 42

Page 17 of 21 Science Advances Manuscript Template

- Cathodes and Cathode Active Materials for Solid-State Batteries. *Advanced Energy Materials n/a* (n/a), 2201425. https://doi.org/10.1002/aenm.202201425.
- 45 (21) Choo, Y.; Hwa, Y.; Cairns, E. J. A Review of the Rational Interfacial Designs and Characterizations for Solid-State Lithium/Sulfur Cells. *Electrochemical Science Advances n/a* (n/a), e2100154. https://doi.org/10.1002/elsa.202100154.

49 50

51

52

53

54

55

56

57

58

59

60

61

62 63

64

65

66

67

68

76

77

78 79

- (22) Combs, S. R.; Todd, P. K.; Gorai, P.; Maughan, A. E. Editors' Choice—Review—Designing Defects and Diffusion through Substitutions in Metal Halide Solid Electrolytes. *Journal of The Electrochemical Society* **2022**, *169* (4), 040551. https://doi.org/10.1149/1945-7111/ac5bad.
- (23) Jung, S.-K.; Gwon, H.; Yoon, G.; Miara, L. J.; Lacivita, V.; Kim, J.-S. Pliable Lithium Superionic Conductor for All-Solid-State Batteries. *ACS Energy Lett.* **2021**, *6* (5), 2006–2015. https://doi.org/10.1021/acsenergylett.1c00545.
- (24) Sörensen, T.; Leeb, S.; Danielsson, J.; Oliveberg, M. Polyanions Cause Protein Destabilization Similar to That in Live Cells. *Biochemistry* **2021**, *60* (10), 735–746. https://doi.org/10.1021/acs.biochem.0c00889.
- (25) Angell, C. A.; Ngai, K. L.; McKenna, G. B.; McMillan, P. F.; Martin, S. W. Relaxation in Glassforming Liquids and Amorphous Solids. *Journal of Applied Physics* **2000**, *88* (6), 3113–3157. https://doi.org/10.1063/1.1286035.
- (26) Aniya, M.; Ikeda, M. A Model for Non-Arrhenius Ionic Conductivity. *Nanomaterials* **2019**, 9 (6). https://doi.org/10.3390/nano9060911.
- (27) Ingram, M. D.; Vincent, C. A.; Wandless, A. R. Temperature Dependence of Ionic Conductivity in Glass: Non-Arrhenius Behavior in the Ag7I4AsO4 System. *Journal of Non-Crystalline Solids* **1982**, *53* (1), 73–82. https://doi.org/10.1016/0022-3093(82)90019-9.
- (28) Li, X.; Liang, J.; Yang, X.; Adair, K. R.; Wang, C.; Zhao, F.; Sun, X. Progress and Perspectives on Halide Lithium Conductors for All-Solid-State Lithium Batteries. *Energy Environ. Sci.* **2020**, *13* (5), 1429–1461. https://doi.org/10.1039/C9EE03828K.
- Zhang, B.; Zhong, J.; Zhang, Y.; Yang, L.; Yang, J.; Li, S.; Wang, L.-W.; Pan, F.; Lin, Z. 69 Discovering a New Class of Fluoride Solid-Electrolyte Materials via Screening the Structural 70 **Property** of Li-Ion Sublattice. Nano Energy 2021, 79, 105407. 71 https://doi.org/10.1016/j.nanoen.2020.105407. 72
- 73 (30) Tomita, Y.; Ohki, H.; Yamada, K.; Okuda, T. Ionic Conductivity and Structure of Halocomplex Salts of Group 13 Elements. *Solid State Ionics* **2000**, *136–137*, 351–355. https://doi.org/10.1016/S0167-2738(00)00491-4.
 - (31) Chapman, R. P.; Bryce, D. L. Application of Multinuclear Magnetic Resonance and Gauge-Including Projector-Augmented-Wave Calculations to the Study of Solid Group 13 Chlorides. *Phys. Chem. Chem. Phys.* **2009**, *11* (32), 6987–6998. https://doi.org/10.1039/B906627F.
- Ash, J. T.; Grandinetti, P. J. Solid-State NMR Characterization of 69Ga and 71Ga in Crystalline Solids. *Magnetic Resonance in Chemistry* **2006**, 44 (9), 823–831. https://doi.org/10.1002/mrc.1841.
- 83 (33) Perras, F. A.; Bryce, D. L. Direct Characterization of Metal–Metal Bonds between Nuclei 84 with Strong Quadrupolar Interactions via NMR Spectroscopy. *J. Phys. Chem. Lett.* **2014**, 5 85 (22), 4049–4054. https://doi.org/10.1021/jz5023448.
- 86 (34) Tanaka, H.; Kobayashi, A.; Saito, T.; Kawano, K.; Naito, T.; Kobayashi, F. H. λ-Type BETS
 87 Salts Containing a Mixed Halide Gallium Anion, GaXx Y4–x⊖ [X, Y = F, Cl, Br; BETS =
 88 Bis(Ethylenedithio)Tetraselenafulvalene]. *Advanced Materials* **1996**, 8 (10), 812–815.
 89 https://doi.org/10.1002/adma.19960081009.
- 90 (35) McGarvey, B. R.; Taylor, M. J.; Tuck, D. G. Gallium-71 NMR Studies of Anionic Gallium 91 Halide Species in Nonaqueous Solution. *Inorg. Chem.* **1981**, 20 (7), 2010–2013. 92 https://doi.org/10.1021/ic50221a015.

Science Advances Manuscript Template Page 18 of 21

- 93 (36) Davidson, G. Elements of Group 3. *Coordination Chemistry Reviews* **1983**, *49*, 117–192. 94 https://doi.org/10.1016/0010-8545(83)80014-9.
- Massiot, D.; Vosegaard, T.; Magneron, N.; Trumeau, D.; Montouillout, V.; Berthet, P.; Loiseau, T.; Bujoli, B. 71GaNMR of Reference GaIV, GaV, and GaVI Compounds by MAS and QPASS, Extension of Gallium/Aluminum NMR Parameter Correlation. *Solid State Nuclear Magnetic Resonance* **1999**, *15* (3), 159–169. https://doi.org/10.1016/S0926-2040(99)00053-3.

01

02

03

04

05 06

07

08

09

14

15

16

17

18

- (38) Kumar, M.; Yamada, K.; Okuda, T.; Sekhon, S. S. Temperature Dependence of 19F NMR and Ion Transport Parameters of Fluoride Ion Conductors SnF2—PbF2 and 2SnF2—NH4F Prepared by Mechanical Milling. *physica status solidi* (*b*) **2003**, 239 (2), 432–438. https://doi.org/10.1002/pssb.200301815.
 - (39) Wang, F.; Grey, C. P. A 1- and 2-D 19F MAS NMR Study of Fluoride-Ion Mobility in α PbF2. *J. Am. Chem. Soc.* **1998**, *120* (5), 970–980. https://doi.org/10.1021/ja972312g.
- (40) Preishuber-Pflügl, F.; Bottke, P.; Pregartner, V.; Bitschnau, B.; Wilkening, M. Correlated Fluorine Diffusion and Ionic Conduction in the Nanocrystalline F– Solid Electrolyte Ba0.6La0.4F2.4—19F T1(Q) NMR Relaxation vs. Conductivity Measurements. *Phys. Chem. Chem. Phys.* **2014**, *16* (20), 9580–9590, https://doi.org/10.1039/C4CP00422A.
- 10 (41) Liu, Y.; Hong, L.; Jiang, R.; Wang, Y.; Patel, S. V.; Feng, X.; Xiang, H. Multifunctional
 11 Electrolyte Additive Stabilizes Electrode–Electrolyte Interface Layers for High-Voltage
 12 Lithium Metal Batteries. *ACS Appl. Mater. Interfaces* **2021**, *13* (48), 57430–57441.
 13 https://doi.org/10.1021/acsami.1c18783.
 - (42) Heitjans, P.; Wilkening, M. Ion Dynamics at Interfaces: Nuclear Magnetic Resonance Studies. *MRS Bulletin* **2009**, *34* (12), 915–922. https://doi.org/10.1557/mrs2009.213.
 - (43) Preishuber-Pflügl, F.; Wilkening, M. Mechanochemically Synthesized Fluorides: Local Structures and Ion Transport. *Dalton Trans.* **2016**, *45* (21), 8675–8687. https://doi.org/10.1039/C6DT00944A.
- 19 (44) Bloembergen, N.; Purcell, E. M.; Pound, R. V. Relaxation Effects in Nuclear Magnetic 20 Resonance Absorption. *Phys. Rev.* **1948**, 73 (7), 679–712. 21 https://doi.org/10.1103/PhysRev.73.679.
- 22 (45) Hanghofer, I.; Brinek, M.; Eisbacher, S. L.; Bitschnau, B.; Volck, M.; Hennige, V.; Hanzu, I.; Rettenwander, D.; Wilkening, H. M. R. Substitutional Disorder: Structure and Ion Dynamics of the Argyrodites Li6PS5Cl, Li6PS5Br and Li6PS5I. *Phys. Chem. Chem. Phys.* 2019, 21 (16), 8489–8507. https://doi.org/10.1039/C9CP00664H.
- 26 (46) Kresse, G.; Furthmüller, J. Efficient Iterative Schemes for Ab Initio Total-Energy Calculations Using a Plane-Wave Basis Set. *Phys. Rev. B* **1996**, *54* (16), 11169–11186. https://doi.org/10.1103/PhysRevB.54.11169.
- 29 (47) Blöchl, P. E. Projector Augmented-Wave Method. *Phys. Rev. B* **1994**, *50* (24), 17953–17979. 30 https://doi.org/10.1103/PhysRevB.50.17953.
- Perdew, J. P.; Burke, K.; Ernzerhof, M. Generalized Gradient Approximation Made Simple. *Phys. Rev. Lett.* **1996**, 77 (18), 3865–3868. https://doi.org/10.1103/PhysRevLett.77.3865.
- Lacivita, V.; Westover, A. S.; Kercher, A.; Phillip, N. D.; Yang, G.; Veith, G.; Ceder, G.; 33 Dudney, N. J. Resolving the Amorphous Structure of Lithium Phosphorus Oxynitride 34 (Lipon). Soc. 2018, 140 (35),11029-11038. 35 J. Am.Chem. https://doi.org/10.1021/jacs.8b05192. 36
- (50) Lacivita, V.; Artrith, N.; Ceder, G. Structural and Compositional Factors That Control the
 Li-Ion Conductivity in LiPON Electrolytes. *Chem. Mater.* 2018, 30 (20), 7077–7090.
 https://doi.org/10.1021/acs.chemmater.8b02812.
- 40 (51) Martínez, L.; Andrade, R.; Birgin, E. G.; Martínez, J. M. PACKMOL: A Package for Building Initial Configurations for Molecular Dynamics Simulations. *Journal of Computational Chemistry* **2009**, *30* (13), 2157–2164. https://doi.org/10.1002/jcc.21224.

Science Advances Manuscript Template Page 19 of 21

- Jain, A.; Ong, S. P.; Hautier, G.; Chen, W.; Richards, W. D.; Dacek, S.; Cholia, S.; Gunter,
 D.; Skinner, D.; Ceder, G.; Persson, K. A. Commentary: The Materials Project: A Materials
 Genome Approach to Accelerating Materials Innovation. *APL Materials* 2013, *1* (1), 011002.
 https://doi.org/10.1063/1.4812323.
- 47 (53) Henkelman, G.; Arnaldsson, A.; Jónsson, H. A Fast and Robust Algorithm for Bader 48 Decomposition of Charge Density. *Computational Materials Science* **2006**, *36* (3), 354–360. 49 https://doi.org/10.1016/j.commatsci.2005.04.010.
 - (54) Tang, W.; Sanville, E.; Henkelman, G. A Grid-Based Bader Analysis Algorithm without Lattice Bias. *Journal of Physics: Condensed Matter* **2009**, *21* (8), 084204. https://doi.org/10.1088/0953-8984/21/8/084204.
 - (55) Pan, H.; Ganose, A. M.; Horton, M.; Aykol, M.; Persson, K. A.; Zimmermann, N. E. R.; Jain, A. Benchmarking Coordination Number Prediction Algorithms on Inorganic Crystal Structures. *Inorg. Chem.* **2021**, *60* (3), 1590–1603. https://doi.org/10.1021/acs.inorgchem.0c02996.
 - (56) Ong, S. P.; Richards, W. D.; Jain, A.; Hautier, G.; Kocher, M.; Cholia, S.; Gunter, D.; Chevrier, V. L.; Persson, K. A.; Ceder, G. Python Materials Genomics (Pymatgen): A Robust, Open-Source Python Library for Materials Analysis. *Computational Materials Science* **2013**, *68*, 314–319. https://doi.org/10.1016/j.commatsci.2012.10.028.

Acknowledgments

Funding:

50

51

52

53

54

55

56

57

58

59

60 61

62

63

64

65

66

67

68

69

70

71

74

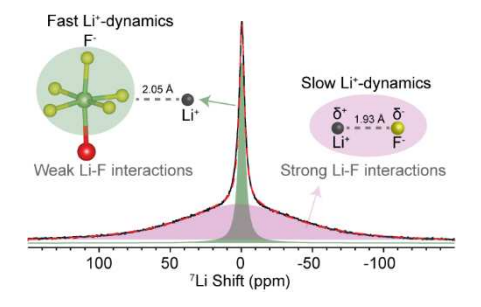
76

77 78

- National Science Foundation grant DMR-1847038
- Samsung Advanced Institute of Technology.
- A portion of this work was performed at the National High Magnetic Field Laboratory, which is supported by National Science Foundation Cooperative Agreement Nos. DMR-1644779 and DMR-2128556* and the State of Florida.

Author Contributions:

- The manuscript was written through the contributions of all authors. All authors have given approval to the final version of the manuscript. †These authors contributed equally.
- 72 Conceptualization: YH, RK, VL
- 73 Methodology: YH, RK, VL
 - Investigation: SVP, VL, HL, ET, YJ, EW, LM, RK, HG, SJ, YH, RK
- 75 Supervision: YH, RK
 - Writing—original draft: SVP, VL, HL, ET
 - Writing—review & editing: YH, VL, RK



79 80

Supplementary Material	Materials	plementary	Suppl
------------------------	-----------	------------	-------

Supporting Information. The supporting information contains ⁷¹Ga DFT calculations and Plot of partial pair distribution functions in one structure model of 2LiI-GaF₃.

Science Advances Manuscript Template Page 21 of 21